

Article

# Population Kinetics Modeling of Low-Temperature Argon Plasma

Hyun-Kyung Chung <sup>1,\*</sup>, Mi-Young Song <sup>1,\*</sup>, Ji-Won Kwon <sup>2</sup>, Myeong-Geon Lee <sup>2</sup>, Jihoon Park <sup>2</sup>, Namjae Bae <sup>2</sup>, Jeamin Song <sup>2</sup>, Gon-Ho Kim <sup>2</sup>, Dipti <sup>3</sup> and Yuri Ralchenko <sup>4</sup>

<sup>1</sup> Korea Institute of Fusion Energy, 169-148 Gwahak-ro, Yuseong-gu, Daejeon 34133, Korea; hkchung@kfe.re.kr

<sup>2</sup> Department of Energy Systems Engineering, Seoul National University, Seoul 08826, Korea;

anakin1229@snu.ac.kr (J.-W.K.); lmg1142@snu.ac.kr (M.-G.L.); wlgntslsqkf@snu.ac.kr (J.P.);

baenj2002@snu.ac.kr (N.B.); woals356@snu.ac.kr (J.S.); ghkim@snu.ac.kr (G.-H.K.)

<sup>3</sup> IAEA Nuclear Data Section Vienna International Centre, P.O. Box 100, 1400 Vienna, Austria; d.dipti@iaea.org

<sup>4</sup> Atomic Spectroscopy Group, National Institute of Standards and Technology, Gaithersburg, MD 20899, USA; yuri.ralchenko@nist.gov

\* Correspondence: mysong@kfe.re.kr

**Abstract:** Optical emission spectroscopy has been widely used in low-temperature argon plasma diagnostics. A coronal model is usually used to analyze the measured line ratios for diagnostics with a single temperature and density. However, many plasma processing conditions deviate from single temperature and density, optically thin conditions, or even coronal plasma conditions due to cascades from high-lying states. In this paper, we present a collisional-radiative model to investigate the validity of coronal approximations over a range of plasma conditions of  $T_e = 1\text{--}4$  eV and  $N_e = 10^8\text{--}10^{13}$  cm<sup>-3</sup>. The commonly used line ratios are found to change from a coronal limit where they are independent of  $N_e$  to a collisional-radiative regime where they are not. The effects of multiple-temperature plasma, radiation trapping, wall neutralization, and quenching on the line ratios are investigated to identify the plasma conditions under which these effects are significant. This study demonstrates the importance of the completeness of atomic datasets in applying a collisional-radiative model to low-temperature plasma diagnostics.

**Keywords:** argon optical emission spectroscopy; plasma processing; coronal models; collisional-radiative model; nonlocal thermodynamic equilibrium plasmas; population kinetics; radiation transport; opacity effects; Non-Maxwellian plasmas



check for updates

**Citation:** Chung, H.-K.; Song, M.-Y.; Kwon, J.-W.; Lee, M.-G.; Park, J.; Bae, N.; Song, J.; Kim, G.-H.; Dipti; Ralchenko, Y. Population Kinetics Modeling of Low-Temperature Argon Plasma. *Atoms* **2021**, *9*, 100. <https://doi.org/10.3390/atoms9040100>

Academic Editor: Grzegorz Piotr Karwasz

Received: 3 November 2021

Accepted: 19 November 2021

Published: 24 November 2021

**Publisher's Note:** MDPI stays neutral with regard to jurisdictional claims in published maps and institutional affiliations.



**Copyright:** © 2021 by the authors. Licensee MDPI, Basel, Switzerland. This article is an open access article distributed under the terms and conditions of the Creative Commons Attribution (CC BY) license (<https://creativecommons.org/licenses/by/4.0/>).

## 1. Introduction

Argon plasmas are widely used for plasma processing applications, and the information on the thermodynamic properties of plasma, such as electron temperature, density, and electron energy distribution function, plays an important role in the control and performance of plasma applications [1–3].

Plasma spectroscopy is a non-intrusive diagnostic technique that provides information on not only the thermodynamic properties of plasma but also the atomic-level population distributions and radiative properties. For many decades, argon optical emission spectroscopy (OES) has been used to obtain electron temperature and density information from the measured line ratios, and more recently, the shape of the electron energy distribution functions [4–7]. For spectroscopic analysis, a population kinetics model should be built to couple the atomic-level population distributions and radiative properties with the plasma thermodynamic properties. For low-electron-density plasmas, a coronal model has been generally adopted to interpret the spectral line intensity distribution [1–3], where an excited atomic state emitting a line of interest is assumed to be populated from the ground state or a metastable state by collisional excitation and depopulated by spontaneous emission to the lower states.

This assumption is valid only if there is no collisional coupling with states other than the ground state, and there are negligible radiative cascades from the upper states. Therefore, the application of the coronal model for spectroscopic analysis is simple, as it requires only collisional excitation rates and spontaneous emission rates of the related atomic transitions. This model has been widely used to explain the emission observed in astrophysical coronal plasmas, tokamak plasmas, and low-density plasmas.

However, the validity of the coronal model may not hold for industrial processing plasmas, even those with relatively low densities. For example, an external electric field is applied in the plasma generation devices of inductively coupled plasma (ICP) and capacitively coupled plasmas (CCP), where electrons tend to have non-Maxwellian energy distributions [8,9]. If high-energy electrons exist as a tail, highly excited states, such as auto-ionizing states and ionized states, may be significantly populated, and the radiative cascades from these states may enhance the population density of the excited states of optical lines. If high-energy electrons are under-populated when compared with the Maxwellian distribution, resulting in the lower-energy electrons being overpopulated, the collisional deexcitation and recombination rates may increase the rate of downward processes.

Radiative self-pumping effects may need to be considered when the plasma size is very large, in the order of centimeters [1–3]. Even if the ion density is low, line opacities can be higher than unity, and the self-pumping effects can reduce the radiative downward processes. In this case, the atomic-level population distribution is a function of the plasma size and, to some degree, the nonlocal plasma conditions. CCP and ICP plasmas may have time dependence in the electron energy distribution function, as some applications use a pulsed-mode operation. Then, the plasma conditions fluctuate over time during the optical measurements, and the observed emission is time integrated. If this is significant, a time-dependent population kinetics model could help test whether the level population distribution converges to a steady-state population within the pulsed operation.

A critical consideration for modeling processing plasmas was found to be the boundary effect, where the atomic state population can be modified by wall contacts. While plasma and material (or wall) interactions are not very well characterized, the diffusion of plasmas near the boundary layer plays a significant role in the population distribution and charge state distribution. It is empirically known that the ground state of a singly ionized argon charge state is neutralized by contact with the wall, and, more importantly, the metastable states of neutral argon atoms are depopulated by contact with the wall. Therefore, the interaction with the wall complicates the analysis, as the population cascades from the high-lying states and the ionized states will be dependent on the wall interaction; moreover, the metastable state population may be quenched [3,10].

A coronal model is a limiting case of a collisional-radiative (CR) model at low density; hence, a general analysis of OES measurements can be performed with a CR model, which includes all relevant atomic processes, beyond a coronal approximation. A well-constructed CR model should provide results consistent with those of a coronal model if the plasma conditions are close to the coronal equilibrium. It has the advantage of allowing the investigation of the validity of coronal approximation for a given plasma condition and identifying the line ratios to provide diagnostic information. Another advantage is that the metastable population distributions are more reliably calculated over a wide range of plasma conditions [11].

In this paper, we present a CR model for near-neutral argon OES and investigate the issues described above for a wide range of plasma conditions. This model is developed based on the principles outlined recently by a nonlocal thermodynamic equilibrium (NLTE) kinetics workshop series [12–18] and a book on the review of NLTE code development over the last 20 years [19]. The atomic datasets and sources used in the model are discussed and evaluated in comparison with the optical measurements. The CR model results are discussed for various non-coronal conditions described above and compared with the existing measurements. This study demonstrates the importance of the completeness of atomic datasets in applying a collisional-radiative model to low-temperature plasma diagnostics.

## 2. Materials and Methods

### 2.1. Construction of a Collisional Radiative (CR) Model

To determine the relationship between the observed emission spectra and plasma thermodynamic properties, we need to obtain the atomic-level population distribution as a function of the plasma thermodynamic properties, as the radiative properties of plasmas, such as spectral emission and absorption, are a function of the atomic level population. The emission coefficient is proportional to the upper-level population of radiative transition, and the absorption coefficient is proportional to the lower-level population distribution minus the upper-level population multiplied by the ratio of the statistical weights. The atomic-level population distribution is determined using collisional processes involving mainly electrons and radiative transitions due to spontaneous radiative processes and stimulated radiative processes by the nonlocal radiation field. In this study, we focus on electron-driven collisional processes while ignoring atom–atom or atom–ion collisions, assuming that the atomic density was substantially low. However, Ar<sub>2</sub> molecular emissions have been observed [3], and such processes involving atomic collisions could be important in understanding population kinetics of processing plasma. An atomic-level population distribution is obtained from a set of time-dependent rate equations, including collisional and radiative transitions, as shown in Equation (1):

$$\frac{dn_i}{dt} = -n_i \sum_{j \neq i}^{N_L} W_{ij} + \sum_{j \neq i}^{N_L} n_j W_{ji}, 1 \leq i \leq N_L, \quad (1)$$

where  $N_L$  is the number of atomic levels considered in the model. The rates between  $i$  and  $j$  states,  $W_{ji}$ , and  $W_{ij}$  are described in Equation (3) in two cases, where the  $i$  state is lower than the  $j$  state.

$$\begin{aligned} W_{ij} &= B_{ij} \bar{J}_{ij} + N_e C_{ij} + \beta_{ij} + N_e \gamma_{ij} + \sigma_{ij} \\ W_{ji} &= A_{ji} + B_{ji} \bar{J}_{ij} + N_e D_{ji} + Q_{ji} + N_e \alpha_{ji}^{RR} + N_e \kappa_{ji}^{EC} + N_e^2 \delta_{ji} + \nu_{ji}. \end{aligned} \quad (2)$$

The collisional and radiative processes considered in the model are as follows: For bound–bound transitions:

- $A_{ji}$  spontaneous emission,
- $B_{ij}$  stimulated absorption ( $i \ll j$ ) or emission ( $i \gg j$ ),
- $C_{ij}$  collisional excitation,
- $D_{ji}$  collisional deexcitation,
- $J_{ij}$  mean radiation field of a unit of energy per squared area per second per photon frequency, and
- $Q_{ji}$  wall quenching of metastable states.

For bound–free transitions:

- $A_{ji}$  spontaneous emission,
- $\alpha_{ij}$  radiative recombination,
- $\beta_{ij}$  photoionization plus stimulated recombination,
- $\gamma_{ij}$  collisional ionization,
- $\delta_{ij}$  collisional recombination,
- $\kappa_{ij}$  electron capture,
- $\sigma_{ij}$  autoionization, and
- $\nu_{ij}$  wall neutralization to the neutral ground state.

Recent advances in CR models have shown that dielectronic recombination (DR) processes play a key role in determining the charge state distribution [17,19]. The process is usually modeled with a substantial number of multiply excited autoionization channels, and a model must include all collisional and radiative processes originating from the autoionization channels. At low densities, the states with a very large principal quantum

number contribute to the DR rate coefficients, and the model becomes prohibitively large. Therefore, for coronal and near-coronal plasmas, the DR rate coefficients have been used instead of detailed counting of the autoionization and electron capture processes. This approach is adopted in this work, and only the bound states were included in the CR model of neutral atom and one singly ionized state.

A non-Maxwellian NLTE kinetics code NOMAD is used to solve the rate equations for the atomic-level population distribution and one-dimensional radiative transport equation in a uniform plasma approximation for spectral intensities and power intensities [20]. This code has many useful options for investigating the atomic population kinetics over a wide range of plasma conditions. It is suitable for time-dependent plasmas or two-temperature Maxwellian plasmas and includes radiation trapping effects for a finite plasma size. Wall neutralization effects are included with an enhanced recombination rate to promote recombination processes from singly ionized argon to neutral argon. Similarly, wall quenching is added to the two metastable states to allow decay to the neutral ground state. With regard to the construction of a CR model for near-neutral argon, only a limited number of atomic states have been reported and evaluated; hence, the rest of required atomic datasets that are required should be obtained through code calculations or widely used empirical data. In this section, atomic data are evaluated to ensure tractability of the CR model.

## 2.2. Atomic Structures

The atomic energy levels of a neutral argon atom are taken from the NIST (National Institute of Standards and Technology atomic spectra database [21]). The highest state included in the NIST database corresponds to the 58d levels that are 15.75558 eV below the continuum limit of 15.7596117 eV. As the most dominant optical emission arises from  $3p^5 4p$ , and spectral emissions from the 8s levels or above are hardly observed, a total of 229 bound levels up to  $3p^5 7h$  levels of neutral argon atoms, and one level of singly ionized argon ion are included in the model. Because the highest level included in the model is 15.65940 eV, there is an approximately 1 eV gap between the highest level in the model and the continuum limit. It will be interesting to include higher- $n$  Rydberg states and evaluate the effects of collisional cascades through these states. It should be noted that such high- $n$  Rydberg states may no longer be bound because of interactions with ions, electrons, and external electric fields [22], and the highest available bound states could lie much lower than the continuum limit in the plasma with large external electric fields. In this study, the autoionizing states are ignored, and the autoionization and electron capture processes are accounted for by including DR rates in the model. Only bound states are included in this model.

## 2.3. Spontaneous Emission

Spontaneous emission rates are key atomic data for OES models, especially for plasma conditions at the coronal limit. This is because the population distribution of excited states is determined by collisional excitation from the ground state and the sum of all possible spontaneous emission rates to lower states. Therefore, a complete set of radiative transitions originating from the level of interest is required. However, there are only a few recommended spontaneous emission rates available in the NIST atomic spectroscopy database for strong lines. For this model, 404 transitions are taken from the NIST database, and 51 transitions are taken from the B-spline R-matrix (BSR) calculations [23]. Additional rates are taken from various sources: multiconfiguration Dirac–Hartree–Fock (MCDHF) data for 1048 transitions [24,25], Los Alamos National Laboratory (LANL) data for 1349 transitions [26], and flexible atomic code (FAC) data for 15,265 transitions [27]. Available transitions from the ATBASE code developed at the University of Wisconsin (WISC) are also added [28]. The LANL data are calculated by the LANL group by using the Hartree–Fock method proposed by Cowan [29], and the FAC data are calculated by solving the Dirac equations in the  $jj$  coupling scheme by using a parametric potential. The

ATBASE code is also based on the Cowan code. Owing to the lack of electron correlation, the FAC data are known to show poor agreement with other code results or experiments for neutral atom cases. Comparisons among the available datasets show that the accuracy of the FAC data varies over a range.

The oscillator strengths and ratios with the NIST evaluated data, where available, are listed along with the data sources in Tables 1–6 for dominant radiative transitions from Paschen 2p<sub>3</sub>, 2p<sub>1</sub>, 3p<sub>9</sub>, 3p<sub>6</sub>, 3p<sub>1</sub>, and 5p<sub>5</sub> levels to lower levels. For example, the Paschen notation, the 2p<sub>1</sub> level refers to 3p<sub>5</sub>(2P<sub>1/2</sub><sup>o</sup>)4p<sup>2</sup>[1/2]<sub>0</sub>, and 3p<sub>1</sub> level refers to 3p<sub>5</sub>(2P<sub>1/2</sub><sup>o</sup>)5p<sup>2</sup>[1/2]<sub>0</sub>. The oscillator strengths of the radiative transitions from the Paschen 2p levels to 1s levels are found to be comparable for all sources within a factor of 2. The MCDHF data differ within a factor of two from the NIST or BSR data for most transitions. However, there are a few outliers in the LANL and FAC datasets. For high-lying levels, such as the 3p levels, the agreement is far from reasonable (marked in red) and differs by a factor of at least 10, especially for the transitions of 3d levels. For the 5p<sub>5</sub> level, the problem is even worse because there are only two published datasets (from NIST and MCDHF), while the remaining datasets contain FAC data for which the accuracy is not guaranteed.

The credibility of the oscillator strength and, therefore, the spontaneous emission rate data is a serious concern not only for collisional radiative models but also for coronal models. In the coronal model, the level population distribution and line ratio analysis are simple functions of the collisional excitation rate from the ground state and the total spontaneous emission rate from the upper level. Denoting the upper-level population as *N<sub>u</sub>* and the ground level population as *N<sub>g</sub>*, *N<sub>u</sub>* is written as a function of the collisional excitation rate *C<sub>gu</sub>* and the sum of all spontaneous emission rates to the lower level *j* *A<sub>uj</sub>* as follows:

$$N_u = N_g \frac{C_{gu}}{\sum_j A_{uj}}. \tag{3}$$

The uncertainty in *A<sub>uj</sub>* influences the determination of the level population distribution and, therefore, the line ratio analysis. The issue of uncertainties in the spontaneous emission rates is demonstrated in Section 3.1, where the sensitivities of different CR models are discussed.

**Table 1.** Oscillator strengths of neutral argon levels (2p3). The top row contains the upper level, and the 1st column contains the lower level. The 2nd column shows the oscillator strength, the 3rd column shows the ratio of various sources to the evaluated NIST or BSR values, and the 4th column shows the data source. The ratios deviating substantially from unity are marked in red.

2p3											
	$\Omega$	Ratio	Data Source		$\Omega$	Ratio	Data Source		$\Omega$	Ratio	Data Source
	0.029		NIST		0.115		NIST		0.394		BSR
	0.037	1.31	MCDHF		0.150	1.30	MCDHF		0.494	1.25	MCDHF
1s5	0.021	0.74	LANL	1s4	0.109	0.95	LANL	1s2	0.528	1.34	LANL
	0.036	0.96	WISC		0.124	0.83	WISC		0.445	0.90	WISC
	0.047	2.21	FAC		0.146	1.34	FAC		0.317	0.60	FAC

**Table 2.** Oscillator strengths of neutral argon levels (2p1) from various sources. The ratios deviating substantially from unity are marked in red.

2p1							
	$\Omega$	Ratio	Data Source		$\Omega$	Ratio	Data Source
1s4	0.0005		NIST	1s2	0.1250		NIST
	0.0011	2.10	MCDHF		0.1529	1.22	MCDHF
	0.0052	9.87	LANL		0.1494	1.20	LANL
	0.0030	2.71	WISC		0.1350	0.88	WISC
	0.1088	20.97	FAC		0.0021	0.01	FAC

**Table 3.** Oscillator strengths of neutral argon levels (3p9) from various sources. The ratios deviating substantially from unity are marked in red.

3p9											
	$\Omega$	Ratio	Data Source		$\Omega$	Ratio	Data Source		$\Omega$	Ratio	Data Source
1s5	0.004		NIST	3d4'	0.073		NIST	3d1''	0.112		LANL
	0.006	1.75	LANL		0.209	2.87	LANL		0.004	0.04	WISC
	0.005	1.40	WISC		0.180	2.47	WISC		0	0	FAC
	0.007	1.19	FAC		0.029	0.39	FAC		0.718		MCDHF
3d3	0.007		NIST	3d4	0.083		LANL	2s5	0.651	0.91	LANL
	0.000	0.01	LANL		0.060	0.72	WISC		0.715	1.00	WISC
	0.009	1.30	WISC		0.003	0.03	FAC		0.936	1.30	FAC

**Table 4.** Oscillator strengths of neutral argon levels (3p6) from various sources. The ratios deviating substantially from unity are marked in red.

3p6											
	$\Omega$	Ratio	Data Source		$\Omega$	Ratio	Data Source		$\Omega$	Ratio	Data Source
1s5	0.004		NIST	3d4	0.092		LANL	3d2	0.000		LANL
	0.006	1.59	LANL		0.088	0.95	WISC		0.001	2.17	WISC
	0.005	1.38	WISC		0.001	0.01	FAC		0.000	0.84	FAC
	0.002	0.43	FAC		0.011		LANL		0.002		LANL
1s4	0.001		NIST	3d1''	0.004	0.35	WISC	3s1''''	0.009	5.74	WISC
	0.001	0.98	LANL		0.015	1.34	FAC		0.000	0.22	FAC
	0.002	1.41	WISC						0.008		LANL
1s2	0.003	1.88	FAC	2s5	0.416		MCDHF	3s1''	0.001		WISC
	0.000		NIST		0.358	0.86	LANL		0.118		LANL
	0.000	1.46	LANL		0.389	0.94	WISC		0.042	0.36	WISC
3d5	0.000	8.03	FAC	2s4	0.235	0.66	FAC	3s1''''	0	0	FAC
	0.053		LANL		0.006		MCDHF		0.201		MCDHF
	0.036	0.68	WISC		0.008	1.29	LANL		0.173	0.86	LANL
3d3	0.010	0.18	FAC	2s2	0.008	1.26	WISC	3s1''''	0.215	1.07	WISC
	0.162		LANL		0.698	85.31	FAC		0.004	0.02	FAC
	0.077		WISC						0.019		LANL

**Table 5.** Oscillator strengths of neutral argon levels (3p1) from various sources. The ratios deviating substantially from unity are marked in red.

3p1											
	$\Omega$	Ratio	Data Source		$\Omega$	Ratio	Data Source		$\Omega$	Ratio	Data Source
1s4	0.00001		BSR	2s4	0.19130		MCDHF	2s2	0.0037		MCDHF
	0.00015	13.90	LANL		0.17222	0.90	LANL		0.0016	0.43	LANL
	0.00391	358.26	FAC		0.16800	0.88	WISC		0.0080	2.15	WISC
1s2	0.00361		NIST	3d2	0.11080	0.64	FAC	3s1'	0.0761	20.48	FAC
	0.00660	1.83	LANL		2.088e <sup>-16</sup>		LANL		0.2024		LANL
	0.00600	1.66	WISC		0.01800	8617.39	WISC		0.0340	0.17	WISC
	0.00448	0.68	FAC		0.01256	6013.02	FAC				

**Table 6.** Oscillator strengths of neutral argon levels (5p5) from various sources. The ratios deviating substantially from unity are marked in red.

5p5											
	$\Omega$	Ratio	Data Source		$\Omega$	Ratio	Data Source		$\Omega$	Ratio	Data Source
1s4	0.0010		FAC	3s1'	0.0067		FAC	5d5	0.0569		FAC
1s2	0.0003		NIST	3s4	0.0014		FAC	4s4	0.2336		MCDHF
	0.0016	4.98	FAC	4d2	0.0007		FAC		0.0416	0.18	FAC
3d1	0.0002		FAC	4s1'	0.1134		FAC	5d2	0.2246		FAC
2s2	0.0059		FAC	3s1	0.0974		FAC				

#### 2.4. Collisional Excitation

Collisional excitation cross-sections are taken from the following five data sources available at the LXCAT website (<https://fr.lxcat.net>, accessed on 2 November 2021) in addition to the LANL and FAC data: Biagi [30], BSR [31], IST [32], Puech [33], and NGFSRDW [34]. Measured optical emission cross-sections [35–37] have been frequently used in OES analyses. Apparent cross-sections or optical emission cross-sections are not appropriate for use in the CR model, as these cross-sections include population cascades from other levels. These can be used under strictly coronal conditions; however, only direct cross-sections should be considered in the CR model. The BSR data are known to be most accurate for neutral and near-neutral systems, and the data for neutral argon have been favorably evaluated through cross-section measurements of metastable and ground state excitation to 4p levels by Boffard et al. [3]. However, the available BSR data [31] are limited to the Paschen 3s (3p<sup>5</sup> 5s) levels. Paschen 3p (3p<sup>5</sup> 5p) data from the Puech database by Puech and Torchin [33] and the IST data (IST-Lisbon database) [32] are available. A few transitions to 3p<sup>5</sup> 4d, 5d, and 6d levels from the ground state are available from the Biagi database [30]. NGFSRDW data are calculated by the relativistic distorted wave (RDW) method [34], and either the distorted wave calculations or first-order many body theory are used. The distorted wave method is used for the FAC data. A perturbative approach, such as RDW/DW methods, produces larger direct cross-sections when compared with the BSR cross-sections, even when the BSR includes resonance contributions by cascades through highly excited states.

The cross-sections of a few transitions are compared for eight data sources for the low-lying levels in Figure 1. The comparison shows that the cross-sections differ by a factor of two or more for most transitions in different data sources. A better agreement is found for forbidden transitions, but, for most transitions, the agreement is not good. The BSR data

tend to lie below most other data sources, and the NGFSRDW and Boffard data generally lie higher than the other data. Perturbative methods are known to provide slightly higher cross-sections than non-perturbative methods, such as the R-matrix method. The FAC data show fast-decaying cross-sections. At the temperatures of interest, 0.5 eV–3 eV, the threshold values determine the rate coefficients. This is problematic, as transition data involving high-lying levels are only available from the FAC data calculated from the distorted wave method, which is known to be less accurate near threshold values and more accurate at high energies. The FAC data are scaled down by a factor of 10 after comparing them with higher quality datasets for the available transitions. Van Regemorter cross-sections are used if the oscillator strengths are available [38]. In this model, we adopted the BSR dataset as the base dataset and used other data sources for the missing transition data in the order of Biagi, Puech, IST, Boffard, NGFSRDW, LANL, and FAC. Van Regemorter cross-sections were also compared and used for the missing transition data. As demonstrated in Section 3.1, the level population distribution and line ratios are sensitive to the completeness of the collisional transition data, as well as the accuracy of the data.

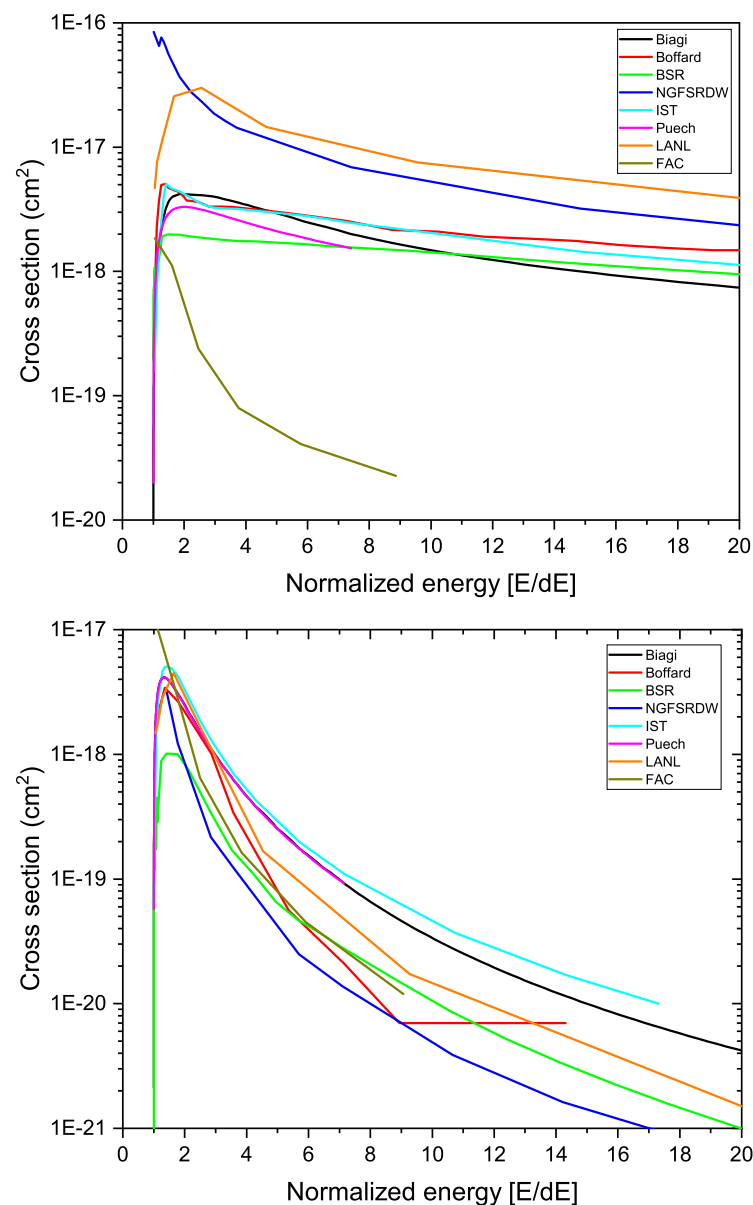


**Figure 1.** Comparison of collisional excitation cross-sections from the ground state to Paschen levels  $2p_1$  (upper) and  $3d'_4$  (forbidden transition) (lower) for various available sources.



### 2.5. Ionization and Recombination

Bound-free transitions, collisional ionization, radiative recombination, dielectronic recombination (DR), and collisional recombination are considered in the model. The ionization rate coefficient from the ground state is taken from the Biagi database. The BSR and LANL cross-sections are compared with the Lotz formula [39]. The DR rate coefficient is obtained from Mazzotta et al. [40]. FAC datasets are used for the collisional ionization data and radiative recombination data for all excited states.

## 3. Results

### 3.1. Sensitivity to Model Completeness

Six CR models, shown in Table 7, are compared to demonstrate the sensitivity of the line ratio analysis to the scope and completeness of the atomic datasets used in the model. Base model A utilizes BSR, Biagi, and Puech collisional data from LXCAT and Van Regemorter cross-sections [38] using NIST oscillator strengths (NIST-VR). LANL and FAC refer to collisional data by LANL code and FAC code. MCDHF-VR/LANL-VR/FAC-VR refers to Van Regemorter collisional data using the MCDHF/LANL/FAC oscillator strengths. MCDHF-GF/LANL-GF/FAC-GF refers to the MCDHF/LANL/FAC oscillator strengths to be used in addition to the NIST oscillator strengths. Model B adds LANL/FAC collisional data in addition to the base model A. Model C adds oscillator strengths from MCDHF and LANL code to model B. Model D adds oscillator strengths from the FAC code to model C. Model E utilizes the base model A and adds only Van Regemorter collisional data using MCDHF/LANL/FAC oscillator strengths. Model F is our final and most complete model, as well as includes the LANL/FAC collisional data and Van Regemorter data using the available oscillator strengths.

**Table 7.** Total number of transitions included in the 6 models.

A		B		C	
BSR	441	A model	768	B model	17,256
Biagi	11	LANL	846	MCDHF-GF	999
Puech	10	FAC	15,411	LANL-GF	999
NIST-VR	306	Total	17,256	Total	18,255
Total	768				
D		E		F (Complete Model)	
C model	18,255	A model	768	D model	30,787
FAC-GF	12,532	MCDHF-VR	496	MCDHF-VR	496
Total	30,787	LANL-VR	624	LANL-VR	624
		FAC-VR	13,937	FAC-VR	13,937
		Total	15,825	Total	45,844

The calculated line ratios of 425.9 nm/750.4 nm analyzed by Boffard et al. [1] are compared to demonstrate the sensitivities of the CR model to the model completeness. The 425.9 nm line corresponds to the transition between  $3p^5(2P_{1/2}^{\circ})4s^2[1/2]_1^{\circ}$  (Paschen  $1s_2$ ) and  $3p^5(2P_{1/2}^{\circ})5p^2[1/2]_0$  (Paschen  $3p_1$ ) states. The upper level Paschen  $3p_1$  level is populated from the ground state, and the cross-section is provided by the Puech data. The 750.4 nm line corresponds to the transition between  $3p^5(2P_{1/2}^{\circ})4s^2[1/2]_1^{\circ}$  (Paschen  $1s_2$ ) and  $3p^5(2P_{1/2}^{\circ})4p^2[1/2]_0$  (Paschen  $2p_1$ ) states. The upper-level Paschen  $2p_1$  level is populated from the ground state, and the cross-section is provided by the BSR data. The cross-sections to the upper levels  $3p_1$  and  $2p_1$  from the ground state stay the same for all 6 models; however, the line ratio of 425.9 nm/750.4 nm changes significantly, as the additional transitions to other levels are included in the model. In Figure 2, the line ratios

are plotted as a function of the electron temperature  $T_e$  and electron density  $N_e$  of  $10^8 \text{ cm}^{-3}$ . The addition of LANL/FAC collisional data in model B do not change the line ratio of 425.9 nm/750.4 nm significantly. However, when the oscillator strengths (i.e., spontaneous emission rates) of the MCDHF/LANL/FAC data are added to the model, the ratio decreased by more than a factor of 2. As the additional oscillator strengths are included for Van Regemorter rates, the ratio decreased even further, and the results are closer to the measured data [41,42] in Section 4.1 and to the calculations performed using the measured optical emission cross-sections by Boffard et al. [1]

The comparison in Figure 2 shows the importance of including all relevant spontaneous emission rates when calculating the line ratios at the coronal conditions, such as  $N_e = 10^8 \text{ cm}^{-3}$  considered here. Figure 3 shows quite different trends in the line ratio comparisons at  $N_e$  of  $10^{13} \text{ cm}^{-3}$ , the highest density case of this investigation. The line ratio is much closer among different models, as collisions make the level population distributions deviate from the coronal limit by increasing the collisional depopulation to be comparable with the spontaneous emission rates. All five models (model B–model F) are closer to the measured data [41,42] in Section 4.1, slightly below the coronal calculations of Boffard et al. [1].

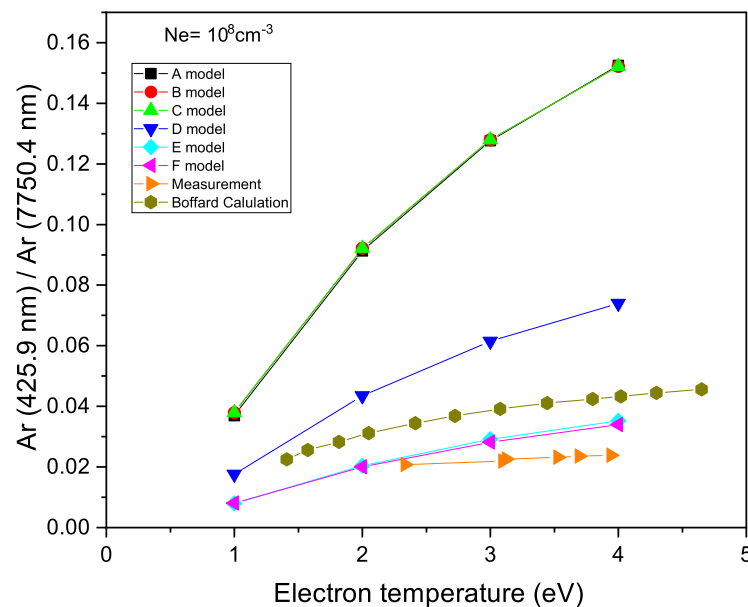


**Figure 2.** Line ratios of Ar 425.9 nm and 750.4 nm as a function of  $T_e$  at  $N_e = 10^8 \text{ cm}^{-3}$  for six models considered in this work. Simulation results were compared with the calculations by Boffard et al. [1] and the measured data [41,42].

A CR model should converge to a coronal limit if  $N_e$  is sufficiently low and the line ratio is independent of  $N_e$ . However, as  $N_e$  increases, the line ratio deviates from the ratio at the coronal limit, as demonstrated for the line ratio of Ar 357.2 nm/Ar 425.9 nm in Figure 4. The transition at Ar 357.2 nm corresponds to the transition between the  $3p^5(2P_{1/2}^o)4s^2[1/2]_1^o$  (Paschen  $1s_2$ ) and  $p^5(2P_{3/2}^o)7p^2[1/2]_0$  (Paschen  $5p_5$ ) states. Unfortunately, there is no reliable collisional data from the ground state to the  $5p_5$  level, except for the measured optical emission cross-section for the transition from the  $5p_5$  level to the  $1s_2$  level. The optical emission cross-section is  $4.6 \times 10^{-20} \text{ cm}^2$  at 25 eV [35]. The direct excitation cross-section is related to the sum of all optical emission cross-sections of transitions originating from the  $5p_5$  level, as follows. The branching ratio of the 357.2 nm transition is roughly 1/3; hence, a factor of 3 may be chosen as the apparent cross-section of the  $5p_5$  level. Then, the apparent cross-section is the sum of the direct cross-section and cascade contribution, and the direct cross-section should be greater than  $4.6 \times 10^{-20} \text{ cm}^2$  but smaller than 3 times  $4.6 \times 10^{-20} \text{ cm}^2$ . Hence, the BSR cross-section was scaled to

be approximately  $8.5 \times 10^{-20} \text{ cm}^2$  at 25 eV was used. The line ratios are compared with the measurements and calculations by Boffard et al. [1] in Figure 4 as a function of Ne. All 6 models showed very large differences in the results of the line ratio of Ar 357.2 nm/Ar 425.9 nm at  $T_e = 2 \text{ eV}$ . The decreasing trend of the line ratio with  $N_e$  agrees with the Boffard data.

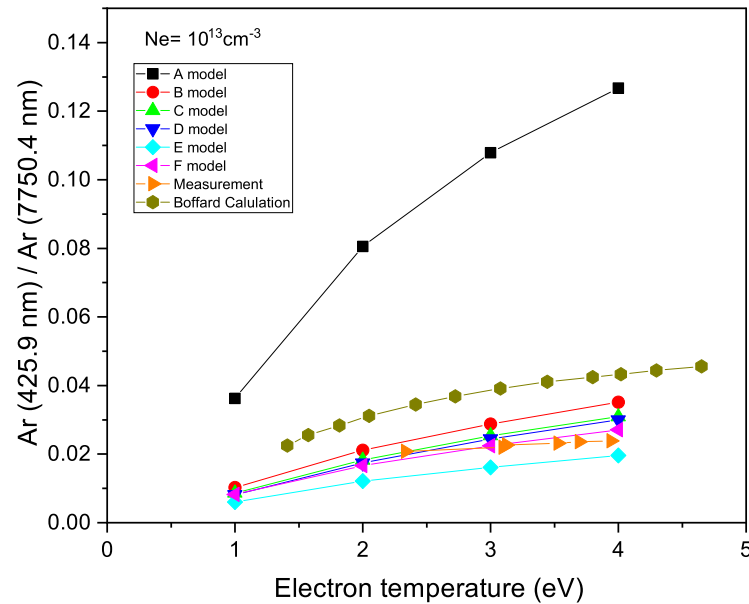


Figure 3. Line ratios of Ar 425.9 nm and 750.4 nm as a function of  $T_e$  at  $N_e = 10^{13} \text{ cm}^{-3}$  for the six models considered in this work. Simulations were compared with calculations by Boffard et al. [1] and the measured data [41,42].

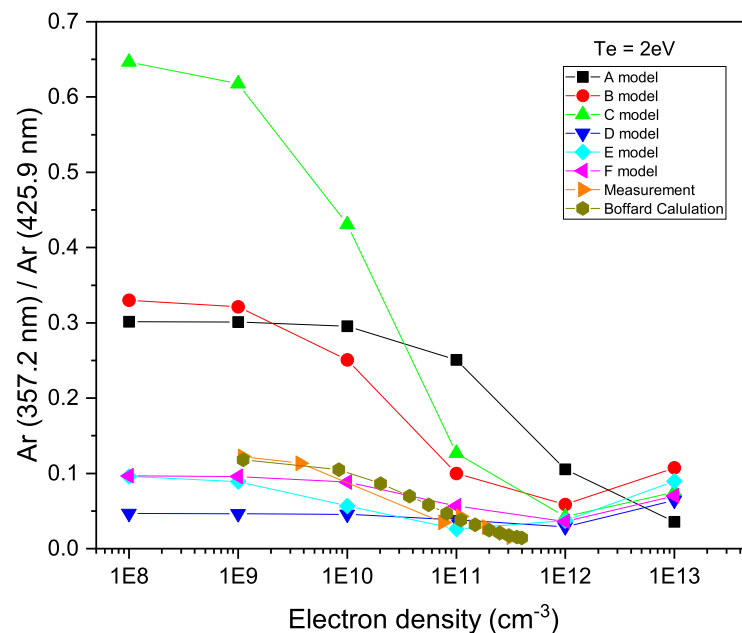


Figure 4. Comparison of line ratios of Ar 357.2 nm and 425.9 nm between simulations and values reported by Boffard et al. [1] at  $T_e = 2 \text{ eV}$ .

The most complete model F agrees best with the Boffard data, although the absolute value differs by approximately 20–30%. This is likely to be attributed to the uncertainties in the spontaneous emission rates, as well as collisional rates involving the  $5p_5$  level, as most transition data involving this level are from the FAC code. Although quite sensitive to  $N_e$ , the line ratios are found to be insensitive to  $T_e$  under 4 eV, the maximum temperature

considered in the simulations. In the following results, we use the most complete model F as our model for discussion.

### 3.2. Radiation Trapping Effects

The effects of radiation trapping on the line intensities and ratios are discussed in the context of the measured pressure dependence of optical emission cross-sections for the selected levels of Ar by Boffard et al. [1]. Radiation trapping for Paschen  $2p_x - 1s_y$  ( $x = 1 - 10, y = 2 - 5$ ) lines is attributed to the large number of atoms in the  $1s$  metastable and resonance levels, direct trapping from the ground state, or indirect contributions due to cascades from the higher resonance levels. It was suggested to use Ar  $np_1$  and  $np_5$  levels (both  $J = 0$ ) to avoid the radiation trapping effects because the optical excitation from the metastable state is weak.

The radiation trapping effects are functions of parameters, such as atomic density, thermodynamic conditions, plasma size, line shapes, etc. To investigate the radiation trapping effects, we assume the following: First, the atomic density or gas pressure is the most important parameter influencing the trapping effects, and it is fixed at  $10^{13} \text{ cm}^{-3}$  in our comparison. Second, different  $N_e$  and  $T_e$  will produce different lower level population distributions; therefore, we compare the lines for the same density and temperature to maintain the lower-level population the same for comparison. Third, the length of the line of sight increases the optical depth and, hence, the radiation trapping effect linearly, which allows the comparison of the radiation trapping effect in a straightforward manner. Finally, different line shape profiles can modify the optical depths and, hence, the radiation trapping effect. In this investigation, the line shape is calculated for the Doppler profile and is, therefore, fixed.

Figures 5 and 6 compare the ratios of the line intensities of 451.1 nm and 750.4 nm with (10 cm plasma size) and without the radiation trapping effect as a function of  $T_e$  for the electron densities of  $10^8 - 10^{13} \text{ cm}^{-3}$ . If the radiation trapping effects are insignificant, the ratios of line intensity for the 10 cm case and the optically thin case will be close to unity. The ratios deviate from 1 more significantly for 451.1 nm emitted from the  $2p_5$  level than for 750.4 nm emitted from the  $2p_1$  level for  $N_e$  below  $10^{12} \text{ cm}^{-3}$ . A slight  $T_e$  dependence on the radiation trapping effects was observed in the case of 451.1 nm, and the lower  $T_e$  ratios deviated further away from unity. As  $N_e$  increases further, collisions change the ground and metastable level population significantly, and the combined effects drive the line intensities away from the coronal limit and the optically thin case.

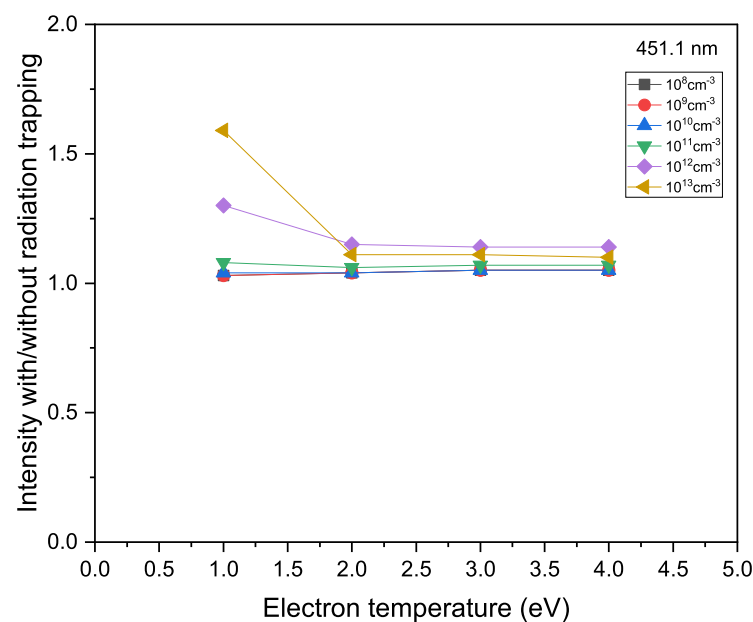


**Figure 5.** Comparison of intensity ratios of 451.1 nm with (10 cm plasma size) and without radiation trapping effect (optically thin case) for different electron densities and temperatures.

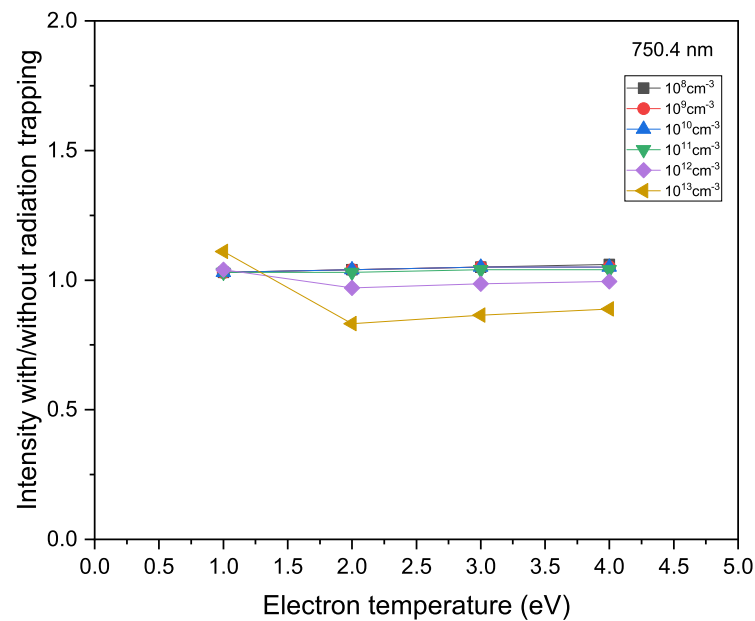


**Figure 6.** Comparison of intensity ratios of 750.4 nm with (10 cm plasma size) and without radiation trapping effect (optically thin case) for different electron densities and temperatures.

In OES analysis, the radiation trapping effects are usually considered with the gas pressure. It is a dominant factor, but the radiation trapping effects should be considered with all factors that influence the population kinetics, for example, gas density,  $N_e$ , and  $T_e$ , as well as the length of the line of sight. In addition, if wall recombination and quenching, or two-temperature distribution effects are combined, the radiation trapping effects may be even more dramatic because these effects modify the lower-level population distribution significantly.

### 3.3. Non-Maxwellian Electron Energy Distributions

Plasmas are frequently found to deviate from a single temperature Maxwellian electron energy distribution. It is useful to understand how line intensities change with non-thermal electron energy distribution functions. We compare two cases: (1) 99% bulk  $T_e$  of 1–4 eV and 1% of 10 eV non-thermal electrons and (2) 60% bulk  $T_e$  of 1–4 eV and 40% of 0.1 eV cold electrons for different electron densities. Radiation trapping was not considered. The first example involves the observation of the effects of 1% 10 eV non-thermal electrons on line ratios of 99% 1–4 eV electron plasmas for a range of electron densities.

Figure 7 shows the ratios of the enhancement due to hot electrons. The ratios of the two lines in the analysis can remain the same if the two line intensities are enhanced by the same factor. In this case, the ratio of the enhancement is close to unity; therefore, the line ratios can be used as a robust diagnostic of the bulk plasma conditions regardless of the existence of small fractions of Non-Maxwellian electrons. Comparing the two line ratios, 357.2 nm/425.9 nm and 425.9 nm/750.4 nm, we find that the former is rather insensitive to the addition of 1% hot electrons, whereas the latter is modified significantly at 1–2 eV. The changes in the ratio become smaller as  $N_e$  becomes higher.

In summary, if  $N_e$  is high and  $T_e$  is high, the effect of 1% 10 eV electrons will be negligible, and the line ratios can be used as a bulk temperature diagnostic. The commonly used line ratios of 425.9 nm/750.4 nm are shown to be more sensitive to the addition of hot electrons; hence, one should be cautious when using this line ratio as a bulk temperature diagnostics. Investigation of the population mechanisms revealed that the cascades from high-lying states are significant for low-lying states, such as  $2p_1$ , the upper level of 750.4 nm. The population cascades increase the enhancement significantly at low temperatures, leading to a large enhancement in the line intensity and deviation from the single  $T_e$  line ratio of 425.9 nm/750.4 nm.

Figure 8 shows that the ratios of line intensity ratios are rather insensitive to the 40% cold electrons when  $N_e$  is sufficiently low. Contrary to the expectation that the line intensities will be reduced due to lower collisionalities, the line intensities are enhanced in the case of 2–4 eV. The ground state population is found to have significantly changed by adding 40% cold electrons in the case of 2–4 eV, where the ground state of neutral atoms is mostly ionized (without wall effects). With the cold electrons, the collisional ionization rate is 40% smaller while radiative recombination and dielectric recombination are higher, which leads to a lower charge state distribution and, hence, higher ground-state population of neutral atoms. Therefore, reduced high-lying and ionized state populations result in reduced cascades from those states and increase the validity of the coronal models for line ratio analysis. The modified line ratios with 40% cold electrons are lower than that in the single temperature case, whereas those with 1% 10 eV non-thermal electrons are generally higher than that in the single temperature case.

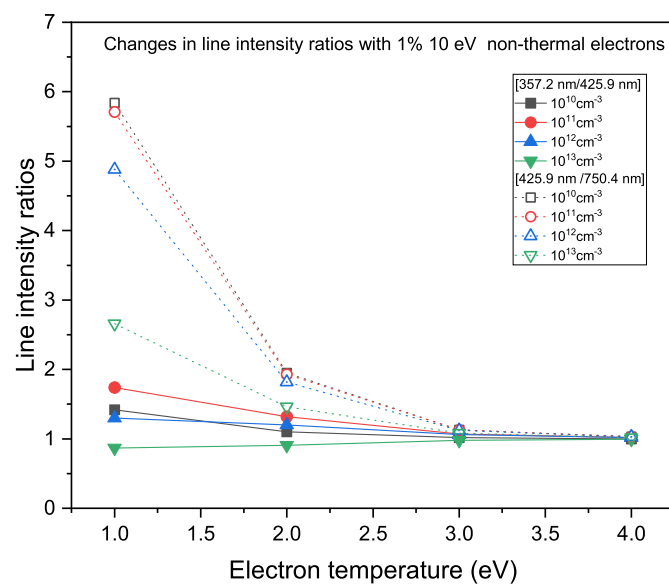


Figure 7. Comparison of the ratios of line ratios of 357.2 nm/425.9 nm and 425.9 nm/750.4 nm with 1% 10 eV non-thermal electrons to those of lines with single-temperature electrons under various plasma conditions.

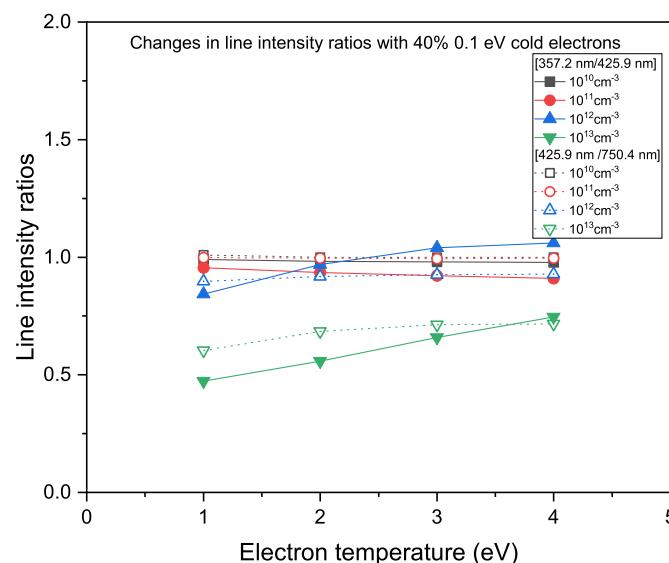


Figure 8. Comparison of the ratios of line intensity ratios of 357.2 nm/425.9 nm and 425.9 nm/750.4 nm when 40% 0.1 eV cold electrons exist to the line ratios with only thermal electrons.

### 3.4. Wall Recombination and Quenching Effects

All the investigations in the previous subsections are performed without considering the boundaries, that is, the wall effects. However, processing plasmas is unique in the sense that the steady-state operation of the plasma is sustained by externally applied fields compensatory energy and particle losses by the wall or boundaries. The main function of the wall in terms of population kinetics is to provide a substantial amount of recombination to the plasma. In general, argon plasmas at 2 eV and  $N_e$  of  $10^{13} \text{ cm}^{-3}$  should ionize substantially to the singly ionized system considering the atomic ionization and recombination rate coefficients. However, Langmuir probe measurements show that the degree of ionization is as low as 1%.

This introduces a difficulty in building a general CR model because the charge balance should be coupled with the diffusion of atoms to the wall and the spatial distribution of plasma conditions established by wall contact [7,10]. Because the diffusion and spatial behavior of plasmas is out of the scope of this work, we focus on the effect of wall recombination on the line ratio analysis. The main influence is the reduction in the charge state population; consequently, the cascades from the ionized states through Rydberg or high-lying states are significantly reduced, as well. To investigate the effect of wall recombination on the line ratios, we added an ad-hoc wall recombination rate to the total recombination rate to make the charge states comparable to those from the Langmuir probe measurements.

As expected from the fact that the wall recombination reduces the ionization, which in turn increases the ground state population, the modified line ratios have similar trends to those in the case of 40% cold electrons, as shown in Figure 9. There is a slight difference in that the enhancement is similar for all lines because only the ground state population changes, whereas, with the 40% cold electrons, the collisional rates change according to the bulk electron temperatures. The ratio of line intensity ratios will be close to unity if the wall effects are negligible. As shown in Figure 9, the commonly used line ratios of 357.2 nm/425.9 nm and 425.9 nm/750.4 nm are not significantly affected by wall recombination for low  $N_e$  cases, where the coronal approximation is relatively good.

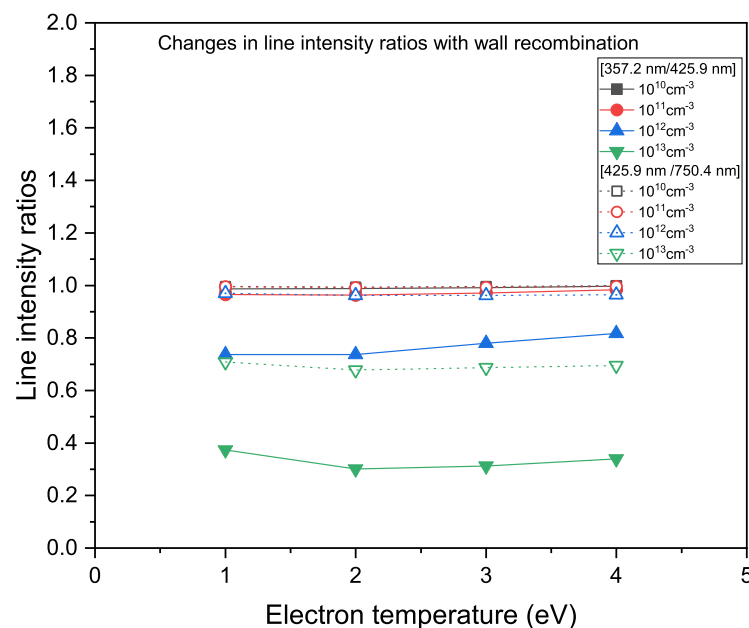


**Figure 9.** Comparison of the ratios of line intensity ratios for 357.2 nm/425.9 nm and 425.9 nm/750.4 nm with wall recombination to the line ratios without wall recombination.

Additionally, it is noted that the wall contact changes the metastable population distributions. Metastable state populations play an important role in stepwise excitation and ionization as  $N_e$  increases. Therefore, the quenching of the metastable population distribution could be very important in line ratio analysis. The wall quenching rate is assumed to be the same as the wall recombination rate, assuming that the wall recombination and quenching rates are a function of the diffusion velocity of particles regardless of their quantum state in this comparison. The results show that the quenching of metastable states did not result in any significantly greater difference than the wall recombination. The line ratios were modified in the same way as that in the case of wall recombination for 357.2 nm, 425.9 nm, and 750.4 nm. It is cautioned that lines sensitive to metastable populations are likely to be affected to a greater extent by wall quenching.

#### 4. Discussion

We use the CR model to analyze OES measurements and discuss spectroscopic diagnostic of low temperature plasmas in this section. The CR models are built using several combinations of atomic datasets described in the previous section. Unfortunately, the uncertainties of the atomic datasets are large, and most transition data beyond the  $3p^5 5s$  levels are not evaluated as discussed in the previous section. Therefore, it is difficult to evaluate the accuracy of the CR model applied to the line-ratio analysis. One may be tempted to choose a set of atomic data to best reproduce the experimental dataset. However, because spectroscopic measurements are influenced by many factors, such as non-thermal electron energy distributions, radiation trapping, wall neutralization and quenching, and collisions with atoms and other impurities in the plasmas, determining the quality of atomic datasets based on plasma spectroscopic measurements is not appropriate. Instead, we investigated the model sensitivities due to different atomic datasets and model completeness and examined the effects of these factors on the line ratio analysis to establish the uncertainties of spectroscopic diagnostics. In this section, we compare our CR model with measurements where the electron density  $N_e$  and temperature  $T_e$  are measured by Langmuir method. This comparison will help identify robust diagnostic line ratios that can be used to collect plasma information. For the simulations discussed below, the plasma conditions are fixed at a gas density of  $10^{13} \text{ cm}^{-3}$ , and the electron density  $N_e$  and temperature  $T_e$  are varied in the range of  $10^8$ – $10^{13} \text{ cm}^{-3}$  and 1–4 eV, respectively. The size of the plasma is zero in all the results, except for the comparisons of the radiation trapping effects, which used a 10 cm plasma size.

##### 4.1. Comparisons with Optical Emission Spectroscopy Measurements

The final and the complete CR model (F model) is compared with the measured line ratios of the spectra from inductively coupled plasma (ICP) and capacitively coupled plasmas (CCP). The capacitively coupled plasmas (CCP) had an argon gas pressure of 20 mTorr and RF power of 200–700 W. The Langmuir probe measurements indicate that the electron densities change from  $1 \times 10^{10} \text{ cm}^{-3}$  to  $2.5 \times 10^{10} \text{ cm}^{-3}$  and electron temperatures stay constant at  $-3.2 \text{ eV}$  over the RF power variation assuming Maxwellian distribution. The inductively coupled plasma (ICP) conditions measured by the Langmuir probe vary from  $5 \times 10^{10} \text{ cm}^{-3}$  to  $2 \times 10^{11} \text{ cm}^{-3}$  and 1.5 to 2.5 eV, depending on the change in gas pressure from 6 mTorr to 20 mTorr. The Langmuir probe measurements for inductively coupled plasma (ICP) and capacitively coupled plasmas (CCP) are shown in Figures 10 and 11, respectively.



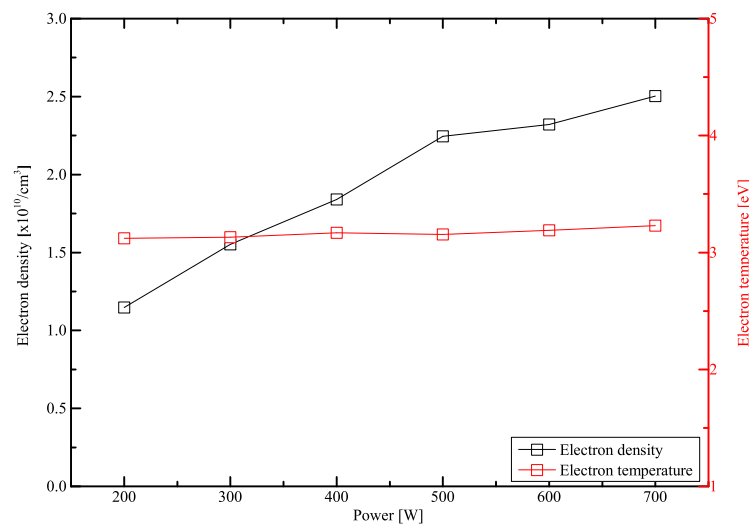


**Figure 10.** Langmuir probe measurements of electron density and temperature as a function of RF power in the CCP plasma. The gas pressure was fixed at 20 mTorr.

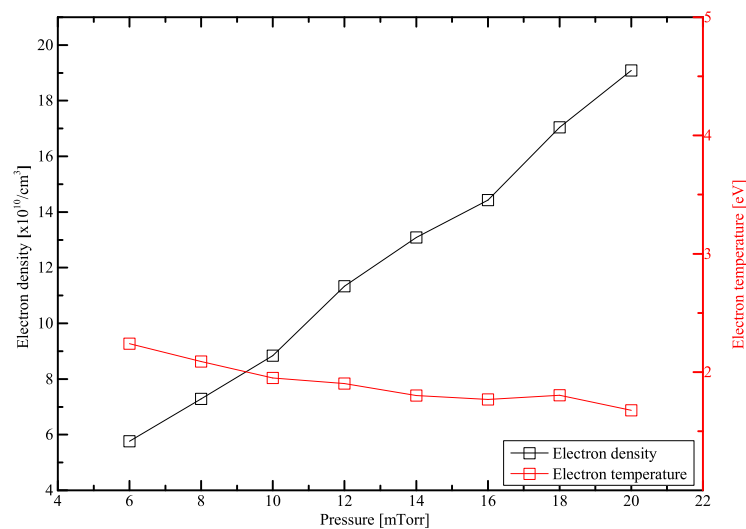


**Figure 11.** Langmuir probe measurements of electron density and temperature as a function of gas pressure in the ICP plasma. The input power was fixed at 500 W.

The CR calculations are performed for the experimental conditions of density and temperature. The plasma size is assumed to be 1.7 cm from the D-gap of 3.4 cm for CCP plasmas, and the wall recombination is added to make the degree of ionization very low, as observed. A single  $T_e$  was assumed. The CR results are compared with the CCP OES data measured from the experimental features in Figure 12. The CR results are compared with the ICP OES data for the 425.9 nm and 750.4 nm line ratios. It is noted that  $N_e$  changes from  $5 \times 10^{10} \text{ cm}^{-3}$  to  $2 \times 10^{11} \text{ cm}^{-3}$ . The line ratio of 425.9 nm and 750.4 nm is sensitive to  $N_e$  above  $1 \times 10^{11} \text{ cm}^{-3}$ . Figure 13 shows the comparison between the CR results and ICP data for  $N_e = 1 \times 10^{10}$  to  $1 \times 10^{12} \text{ cm}^{-3}$  with and without radiation trapping effects. This shows that the dependence of the line ratio on  $N_e$  is different with and without radiation trapping. With radiation trapping, the line ratio increases with  $N_e$ . In contrast, the optically thin cases show that the line ratios decrease with increasing  $N_e$ . The measured line ratios are slightly lower than the CR results. The trend with increasing  $N_e$  (decreasing  $T_e$ ) agrees with the optically thin case.

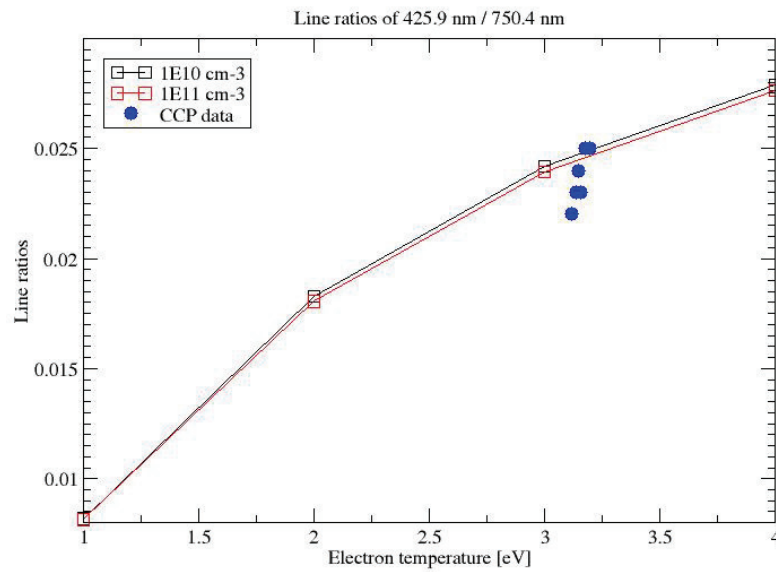


**Figure 12.** Comparison of line ratio of 425.9 nm/750.4 nm between CR results and CCP data for  $N_e = 5 \times 10^{10} \text{ cm}^{-3}$  to  $2 \times 10^{11} \text{ cm}^{-3}$ . A slightly lower  $T_e$  corresponds to a lower  $N_e$  and lower RF power. The measured line ratios have some dependence on  $N_e$ , whereas the simulations do not.

Comparisons with the CCP and ICP data show that the single-temperature CR model predicts the electron density and temperature ranges from the measured line ratios comparable to the Langmuir measurements. The experimental conditions may be included in the CR model as a refinement, such as the multi-temperature cases, different radiation trapping conditions, or wall quenching ratios. However, the calculated line ratios do not change dramatically from the single temperature values. The source of discrepancies between CR results and ICP plasma data below 2 eV needs more investigation.

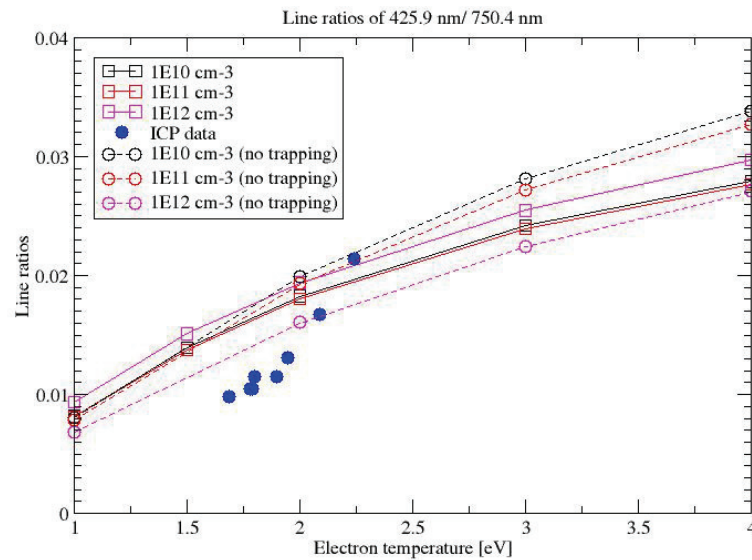


**Figure 13.** Comparison of line ratio of 425.9 nm/750.4 nm between CR results and ICP data for  $N_e = 1 \times 10^{10}$  to  $1 \times 10^{12} \text{ cm}^{-3}$  with and without radiation trapping effects. A lower  $T_e$  corresponds to a higher  $N_e$  value. The optically thin case reproduces the measured line ratios better by producing lower line ratios for higher  $N_e$  values, i.e., above  $1 \times 10^{11} \text{ cm}^{-3}$ .

### 5. Conclusions and Future Work

A CR model employing a complete set of atomic data is constructed to verify the coronal approximation for the OES analysis in plasma processing. Atomic datasets consist

of data from various sources, mainly from NIST atomic spectroscopy databases and LXCAT databases. Low-lying states have relatively reliable atomic data from the evaluated NIST data and BSR collisional data. The data for the high-lying state are provided by the LANL and FAC code data, which introduce uncertainties in the analysis of lines originating from those levels. Comparisons of six models with different atomic datasets show that it is critical to have a complete set of atomic data to ensure reasonable and credible line intensities and, hence, line ratios for application in OES.

A non-LTE kinetics code, NOMAD, is used to solve the rate equations for the level population distributions. The code contains time-dependent population kinetics options, radiation trapping effects, and multi-temperature options. The line ratios change when the radiation trapping effects are included and non-thermal electrons are considered. Wall recombination and quenching do not affect the line ratios if the coronal approximation is valid for the plasma conditions. It is found that, for electron densities  $>10^{12} \text{ cm}^{-3}$ , the plasma is in the CR regime, and the coronal approximation is not valid; therefore, line ratio analysis should consider plasma conditions, such as multi-temperature effects, radiation trapping, wall recombination, and quenching. Comparisons with the CCP and ICP OES measurement show that our CR model yields comparable result with the Langmuir probe measurements of the plasma conditions. In this study, we focus on only a few line ratios analyzed by Boffard et al. [1] and others [2]. In the future, additional line ratios will be studied to provide electron temperature and density diagnostics over a wide range of plasma conditions, particularly with greater focus on wall recombination and quenching rates.

**Author Contributions:** Conceptualization, H.-K.C. and M.-Y.S.; methodology, H.-K.C. and D.; software, H.-K.C.; validation, H.-K.C., M.-Y.S. and G.-H.K.; formal analysis, H.-K.C.; investigation, J.-W.K., M.-G.L., J.P., N.B., J.S.; resources, Y.R.; data curation, J.-W.K., M.-G.L., J.P., N.B., J.S.; writing—original draft preparation, H.-K.C.; writing—review and editing, G.-H.K., M.-Y.S.; visualization, supervision, M.-Y.S.; project administration, M.-Y.S.; funding acquisition, M.-Y.S. All authors have read and agreed to the published version of the manuscript.

**Funding:** This research was supported by the R&D Program of “Plasma BigData ICT Convergence Technology Research Project (code No. 1711124799)” through the Korea Institute of Fusion Energy (KFE) funded by the Government funds, Republic of Korea.

**Institutional Review Board Statement:** Not applicable.

**Informed Consent Statement:** Not applicable.

**Data Availability Statement:** Numerical data for cross sections can be obtained from the authors upon request.

**Acknowledgments:** Not applicable.

**Conflicts of Interest:** The authors declare no conflicts of interest.

## References

1. Boffard, J.B.; Lin, C.C.; DeJoseph, C.A., Jr. Application of excitation cross sections to optical plasma diagnostics. *J. Phys. Appl. Phys.* **2004**, *37*, R143–R161. [[CrossRef](#)]
2. Zhu, X.M.; Pu, Y.K. Optical emission spectroscopy in low-temperature plasmas containing argon and nitrogen: Determination of the electron temperature and density by the line-ratio method. *J. Phys. Appl. Phys.* **2010**, *43*, 403001. [[CrossRef](#)]
3. Donnelly, V.M. Plasma electron temperatures and electron energy distributions measured by trace rare gases optical emission spectroscopy. *J. Phys. Appl. Phys.* **2004**, *37*, R217–R236. [[CrossRef](#)]
4. Boffard, J.B.; Jung, R.O.; Lin, C.C.; Aneskavich, L.E.; Wendt, A.E. Argon 420.1–419.8 nm emission line ratio for measuring plasma effective electron temperatures. *J. Phys. Appl. Phys.* **2012**, *45*, 045201. [[CrossRef](#)]
5. Boffard, J.B.; Jung, R.O.; Lin, C.C.; Aneskavich, L.E.; Wendt, A.E. Optical diagnostics for characterization of electron energy distributions: argon inductively coupled plasmas. *Plasma Sources Sci. Technol.* **2011**, *20*, 055006. [[CrossRef](#)]
6. Dipti.; Gangwar, R.K.; Srivastava, R.; Stauffer, A.D. Collisional-radiative model for non-Maxwellian inductively coupled argon plasmas using detailed fine-structure relativistic distorted-wave cross sections. *Eur. Phys. J.* **2013**, *67*, 203. [[CrossRef](#)]

7. Huh, S.R.; Kim, N.K.; Jung, B.K.; Chung, K.J.; Hwang, Y.S.; Kim, G.H. Global model analysis of negative ion generation in low-pressure inductively coupled hydrogen plasmas with bi-Maxwellian electron energy distributions. *Phys. Plasmas* **2015**, *22*, 033506. [CrossRef]
8. Godyak, V.A. Nonequilibrium EEDF in gas discharge plasmas. *IEEE Trans. Plasma Sci.* **2006**, *34*, 755–766. [CrossRef]
9. Godyak, V.A.; Piejak, R.B. Abnormally low electron energy and heating-mode transition in a low-pressure argon rf discharge at 13.56 MHz. *Phys. Rev. Lett.* **1990**, *65*, 996–999. [CrossRef]
10. Bogaerts, A.; Gijbels, R.; Vlcek, J. Collisional-radiative model for an argon glow discharge. *J. Appl. Phys.* **1998**, *84*, 121–136. [CrossRef]
11. Gangwar, R.K.; Sharma, L.; Srivastava, R.; Stauffer, A.D. Argon plasma modeling with detailed fine-structure cross sections. *J. Appl. Phys.* **2012**, *111*, 053307. [CrossRef]
12. Lee, R.W.; Nash, J.; Ralchenko, Y. Review of the NLTE kinetics code workshop. *J. Quant. Spectrosc. Radiat. Transf.* **1997**, *58*, 737–742. [CrossRef]
13. Bowen, C.; Decoster, A.; Fontes, C.J.; Fournier, K.; Peyrusse, O.; Ralchenko, Y. Review of the NLTE emissivities code comparison virtual workshop. *J. Quant. Spectrosc. Radiat. Transf.* **2003**, *81*, 71–84. [CrossRef]
14. Bowen, C.; Lee, R.; Ralchenko, Y. Comparing plasma population kinetics codes: Review of the NLTE-3 Kinetics Workshop. *J. Quant. Spectrosc. Radiat. Transf.* **2006**, *99*, 102–119. [CrossRef]
15. Rubiano, J.; Florido, R.; Bowen, C.; Lee, R.; Ralchenko, Y. Review of the 4th NLTE Code Comparison Workshop. *High Energy Density Phys.* **2007**, *3*, 225–232. [CrossRef]
16. Fontes, C.; Abdallah, J.; Bowen, C.; Lee, R.; Ralchenko, Y. Review of the NLTE-5 kinetics workshop. *High Energy Density Phys.* **2009**, *5*, 15–22. [CrossRef]
17. Chung, H.K.; Bowen, C.; Fontes, C.; Hansen, S.; Ralchenko, Y. Comparison and analysis of collisional-radiative models at the NLTE-7 workshop. *High Energy Density Phys.* **2013**, *9*, 645–652. [CrossRef]
18. Piron, R.; Gilleron, F.; Aglitskiy, Y.; Chung, H.K.; Fontes, C.; Hansen, S.; Marchuk, O.; Scott, H.; Stambulchik, E.; Ralchenko, Y. Review of the 9th NLTE code comparison workshop. *High Energy Density Phys.* **2017**, *23*, 38–47. [CrossRef] [PubMed]
19. Ralchenko, Y. *Modern Methods in Collisional-Radiative Modeling of Plasmas*; Springer Series on Atomic, Optical, and Plasma Physics; Springer: Berlin/Heidelberg, Germany, 2016. [CrossRef]
20. Ralchenko, Y.; Maron, Y. Accelerated recombination due to resonant deexcitation of metastable states. *J. Quant. Spectrosc. Radiat. Transf.* **2001**, *71*, 609–621. [CrossRef]
21. Kramida, A.; Ralchenko, Y.; Reader, J. NIST Atomic Spectra Database (Ver. 5.5.6). 2018. Available online: <https://www.nist.gov/pml/atomic-spectra-database> (accessed on 2 November 2021).
22. Inglis, D.R.; Teller, E. Ionic Depression of Series Limits in One-Electron Spectra. *Astrophys. J.* **1939**, *90*, 439. [CrossRef]
23. Zatsarinny, O.; Bartschat, K. B-spline calculations of oscillator strengths in neutral argon. *J. Phys. At. Mol. Opt. Phys.* **2006**, *39*, 2145–2158. [CrossRef]
24. Hassouneh, O.; Salah, W. Atomic data of intermediate autoionizing Rydberg series  $nf[KJ]$  ( $n = 4, 5$ ),  $nd[KJ]$  ( $n = 5, 6$ ),  $np[KJ]$  ( $n = 6, 7$ ) and  $ns[KJ]$  ( $n = 7, 8$ ) of neutral argon atom in the multiconfiguration Dirac-Hartree-Fock framework. *Eur. Phys. J. Plus* **2017**, *132*, 312. [CrossRef]
25. Salah, W.; Hassouneh, O. Multiconfiguration Dirac-Hartree-Fock energy levels, oscillator strengths, transition probabilities, hyperfine constants and Landé g-factor of intermediate Rydberg series in neutral argon atom. *Eur. Phys. J. Plus* **2017**, *132*, 160. [CrossRef]
26. LANL. LANL Database. 2018. Available online: <https://www.lanl.gov/collaboration/pathogen-database/index.php> (accessed on 2 November 2021).
27. Gu, M.F. The flexible atomic code. *Can. J. Phys.* **2008**, *86*, 675–689. [CrossRef]
28. Wang, P. *ATBASE User's Guide*; Report No. UWFD-942; University of Wisconsin Fusion Technology Institute: Madison, WI, USA, 1993.
29. Cowan, R.D. *The Theory of Atomic Structure and Spectra*; University of California Press: Berkeley, CA, USA; Los Angeles, CA, USA; London, UK, 1981.
30. BIAGI, S.F. Biagi Database, 2018. Available online: [www.lxcat.net/Biagi](http://www.lxcat.net/Biagi) (accessed on 2 November 2021).
31. Zatsarinny, O.; Bartschat, K. BSR Database. 2018. Available online: [www.lxcat.net/BSR](http://www.lxcat.net/BSR) (accessed on 2 November 2021).
32. Alves, L.L.; Guerra, V. IST-Lisbon Database. 2018. Available online: [www.lxcat.net/IST-Lisbon](http://www.lxcat.net/IST-Lisbon) (accessed on 2 November 2021).
33. Puech, V. Puech Database. 2018. Available online: [www.lxcat.net/Puech](http://www.lxcat.net/Puech) (accessed on 2 November 2021).
34. Stauffer, A. NGFSRDW Database. 2018. Available online: [www.lxcat.net/NGFSRDW](http://www.lxcat.net/NGFSRDW) (accessed on 2 November 2021).
35. Boffard, J.B.; Chiaro, B.; Weber, T.; Lin, C.C. Electron-impact excitation of argon: Optical emission cross sections in the range of 300–2500nm. *At. Data Nucl. Data Tables* **2007**, *93*, 831–863. [CrossRef]
36. Chilton, J.E.; Lin, C.C. Measurement of electron-impact excitation into the  $3p^53d$  and  $3p^55s$  levels of argon using Fourier-transform spectroscopy. *Phys. Rev. A* **1999**, *60*, 3712–3721. [CrossRef]
37. Stewart, M.D.; Chilton, J.E.; Boffard, J.B.; Lin, C.C. Use of radiation trapping for measuring electron-impact excitation cross sections for higher resonance levels of rare-gas atoms. *Phys. Rev. A* **2002**, *65*, 032704. [CrossRef]
38. van Regemorter, H. Rate of Collisional Excitation in Stellar Atmospheres. *Astrophys. J.* **1962**, *136*, 906. [CrossRef]

39. Lotz, W. Electron-Impact Ionization Cross-Sections and Ionization Rate Coefficients for Atoms and Ions. *Astrophys. J. Suppl.* **1967**, *14*, 207. [[CrossRef](#)]
40. Mazzotta, P.; Mazzitelli, G.; Colafrancesco, S.; Vittorio, N. Ionization balance for optically thin plasmas: Rate coefficients for all atoms and ions of the elements H to Ni\*. *Astron. Astrophys. Suppl. Ser.* **1998**, *133*, 403–409. [[CrossRef](#)]
41. Lee, M.-G.; Kwon, J.-W.; Park, J.; Bae, N.; Kim, G.-H.; Chung, H.K. Modeling of Optical Emission Spectroscopy for low temperature Argon plasma. In Proceedings of the 7th International Conference on Microelectronics and Plasma Technology, Incheon, Korea, 25–28 July 2018.
42. Kwon, J.-W.; Lee, M.-G.; Ryu, S.; Jang, Y.; Chung, H.-K.; Song, M.-Y.; Kim, G.H. Effect of High Energy Electron on OES Line Intensity Ratio in Non-Maxwellian Argon Plasmas. In Proceedings of the XXXIV International Conference on Phenomena in Ionized Gases, Sapporo, Japan, 14–19 July 2019.